A Capacitive Backscatter System for Intra-Body Identification

Noor Mohammed, Robert W. Jackson, *Life Fellow, IEEE*, Sunghoon Ivan Lee, *Senior Member, IEEE*, and Jeremy Gummeson

***Abstract*—In this paper, we present a new intra-body communication technology that uses capacitive backscatter. The main goal of this technology is to allow for the transmission of binary IDs between a skin-coupled transceiver and a batteryless tag by utilizing finite conductivity of skin and air coupling capacitance. The intra-body identification (IBID) hardware system consists of two pairs of skin-coupled 50 ohm galvanically isolated electrodes: the interrogator(fixed size: 30 cm × 40 cm) and the tag (arbitrary shape and size). The flexibility of electrode shape enables the IBID tag to be easily deployed on various everyday objects. The interrogator is connected to a battery-powered wearable transceiver. The study investigated the capacitive backscatter phenomenon using two everyday object models: a remote control model and a rectangular single switch panel. The experimental results demonstrate the hardware system's ability to interrogate binary IDs seamlessly using 40 MHz pulsed radio frequency (RF) carrier with 33% duty cycle. However, the variable dimensions of the tag electrode lead to varying path gain within a short body channel, resulting in low available power for the tag. To address this challenge, we developed an ultra-low powered IBID tag that can sustain its operation at −11 *dBm* peak RF power and transmit multiple bursts of 16-bit binary packets.**

***Index Terms*—Intra-body Identification (IBID), capacitive power transfer, backscatter, wireless communication.**

I. Introduction

ENERGY efficient wireless communication between infrastructure and wearable devices is critical in enabling functional body sensor networks. Prior work has focused on active power sources like batteries for both the transceiver and the sensor nodes; however, continuously powering a network of these devices without interrupting their operation remains challenging. The need for frequent recharging and replacement of batteries has led to the demand for batteryless devices that can support both power and communication.

Prior work has leveraged the human body as a medium for wireless power transfer to support battery-free body sensors through Capacitive Intra-Body Power Transfer (C-IBPT) using an on-body RF power source [1], [2], [3]. In a typical C-IBPT setup, the human body and air capacitance allow the displacement current flow by forming a current loop within localized skin-coupled electrodes due to the propagation of low radio frequency (RF) energy within the tens of MHz range from a wearable transmitter.

In addition, communication through the human body has been implemented in simplex mode or half duplex mode, leveraging the unilateral path loss between two battery-powered active devices [4], [5]. This creates a significant challenge in realizing realistic batteryless body sensor networks while simultaneously supporting power transfer and body-centric capacitive radio communication, which have yet to be studied among passive devices.

In this work, we investigate a new intra-body identification (IBID) [6] technology that combines the key technical features of C-IBPT and RF backscatter [7]. Similar to C-IBPT [1], IBID takes advantage of skin conductivity and air coupling capacitance to form the communication loop between a pair of skin-coupled electrodes. In our setting, backscatter communication is established between a batteryless ultra-low power ID tag and a battery-powered, wearable IBID transceiver by modulating the IBID tag's matching network.

One of the practical advantages of the capacitive IBID system is its flexibility in electrode size and shape, allowing it to accommodate different complex geometries. To demonstrate the adaptability of our tag design, we have instrumented two models of daily objects — a remote control and a switch panel as illustrated in Fig. 1. This preliminary study not only reports the physical layer of the IBID technology but also verifies the performance of the custom hardware system, providing a promising glimpse into its suitability for real-world applications.

The key feature of intrabody backscatter is its ability to facilitate capacitive backscatter communication across complex air-skin dielectric mediums, which has not been previously studied. Furthermore, the intrabody backscatter communication needs to consider round-trip path loss, whereas conventional body-coupled capacitive communication only considers a unilateral path loss. To address these two critical technical challenges and enable batteryless wearable sensors or ID tags, we have made the following contributions:

1) We introduce a new hardware architecture for ultra-low-power, batteryless IBID tags that operates at a minimum received peak RF power of 80 uW, achieving an energy efficiency of 0.28 nJ/bit. This represents significant

Received 31 March 2025; revised 8 May 2025; accepted 20 May 2025. Date of publication 27 May 2025; date of current version 11 June 2025. This work was supported in part by the National Science Foundation (NSF) under Grant 016419-00001, and in part by the National Institutes of Health (NIH) under Grant R01HD114147. *(Corresponding author: Jeremy Gummeson.)*

Noor Mohammed, Robert W. Jackson, and Jeremy Gummeson are with the Electrical and Computer Engineering Department, University of Massachusetts Amherst, Amherst, MA 01003 USA (e-mail: noormohammed@umass.edu; jackson@ecs.umass.edu; jgummeso@umass.edu).

Sunghoon Ivan Lee is with the College of Information and Computer Science, University of Massachusetts Amherst, Amherst, MA 01003 USA (e-mail: silee@cs.umass.edu).

Digital Object Identifier 10.1109/JRFID.2025.3574233

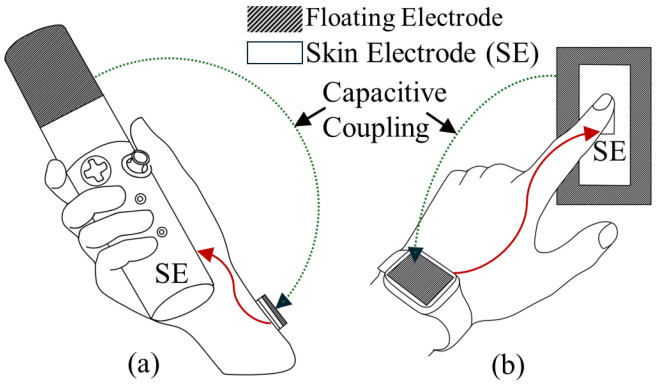

Fig. 1. (a) Remote Controller and (b) switch Panel instrumented for the proposed IBID application.

reduction in power consumption compared to previous RF backscatter systems [7], [8], [9], [10], [11], [12]. This advancement is significant for low channel gain intrabody communication.

2) We developed a custom transceiver to decode a backscattered 16-bit binary ID with a low bit error rate of 10^{-3} and a signal-to-noise ratio (SNR) of 25 to 30 *dB*. The system operates at a 33% duty cycle with a 40 *MHz* RF carrier and a peak power of 19.6 *dBm*, achieving a maximum read range of 28 *cm*, which outperforms in-vivo passive magnetic [11], [13] backscatter systems for implants.
3) We empirically studied performance of the system through a user study (N=10), whereas previous research findings are mostly based on phantom human or animal models [14]. Through these experiments, we quantify power and communication performance across a complex air/dielectric medium.

II. Related Work

RFID backscatter technology has transitioned from simple passive ID tags with limited range to advanced battery-free multipurpose tags [7] with effective communication ranges on the order of centimeters to tens of meters depending on the technology or application. Research has demonstrated significant advancements in backscatter communication, such as ambient RF backscattering with WiFi [12], [15], [16], Bluetooth [9], [16], and LoRa [17]. Specialized applications such as underwater backscatter communications [10], [18] and communication with in-body medical implants [11], [13] have also been explored. These systems exhibit a range of data rates (from tens of bps to several Mbps), operational ranges (from centimeter-scale for implants to tens of meters for Internet of Things (IoT) applications), and power consumption (typically on the order of microwatts). Table I presents a comparative analysis of various backscatter communication systems in terms of operating frequency, data rate, range, receiver's signal-to-noise ratio (SNR), bit error rate (BER), tag's power consumption, and energy consumption per bit.

A. RF Backscatter

Previous work on ambient RF [19] backscatter systems have primarily operated at sub-GHz frequencies, such as 539 *MHz*, with a relatively low power consumption of 0.79 *uW* (TX: 0.25 *uW*, RX: 0.54 *uW*). However, these systems are constrained by a limited range of 0.15 *m* to 1.07 meters and exhibit a high bit error rate (BER) of up to 0.7 (Table I). In contrast, Bluetooth Low Energy (BLE) [9] backscatter achieves a significantly higher data rate of 1 *Mbps*, but this comes at the expense of increased power consumption at 1557.5 *uW* and a limited range of 1 to 30 *m* compared to the WiFi backscatter system [15]. Similarly, the Wireless Identification and Sensing Platform (WISP) [7] provides moderate data rates of 70 *kbps* with a large power requirement of 1080 *uW*. Solutions such as F-S backscatter [20], FreeRider [16], and WiFi [15] Backscatter offer practical mid-range options with improved energy efficiency. For instance, F-S backscatter achieves an energy consumption of 0.91 nJ/bit. On the other hand, LoRa Backscatter is optimized for ultra-long-range applications, reaching distances of up to 2.8 *km* with minimal power requirements of just 9.25 *uW*. Lastly, MIXIQ utilizes a 2.4 *GHz* WiFi backscatter to achieve high data rates of 1.125 *Mbps* but consumes more power at 300 *uW*.

Unlike many RF-based approaches, IBID operates at a frequency of 40 *MHz* using a pulsed carrier, which is less power hungry than the ultra-high frequency (UHF) transmitters used in conventional RFID technology [7], [19] to compensate for free space path loss of more than −60 *dB* (round trip loss). In contrast to general-purpose RF tags, which often face substantial attenuation when passing through conductive human tissues, the IBID tag addresses intrabody communication challenges using impedance-matched wearable electrodes.

B. Underwater Backscatter

For specialized underwater applications, underwater backscatter [10], [18] can achieve communication ranges up to 62 *m* using ultrasound transducers. Note that, due to lossy nature of water, sound energy modalities are typically used in underwater environment which requires specialized piezoelectric transducers. However, it requires higher power levels ranging from 120 to 500 *uW* compared to the radio frequency based solutions.

Similar to underwater backscatter, IBID implements a new hardware architecture that operates across a relatively under-explored complex dielectric medium comprising both human tissue and air while achieving robust communication performance.

C. Magnetic Backscatter

Magnetic [11] backscatter enables reliable in-body communication with a significantly lower BER of less than 10^{-3} and a higher power requirement of 730 *uW*. On the other hand, magneto-electric [13] backscatter offers an alternative with a very low power consumption of just 10 *nW* while maintaining a short range of around 2 *cm*.

While magnetic backscatter enables power and communication for health sensors, IBID is more well-suited for wearable

TABLE I
COMPARISON OF BACKSCATTER COMMUNICATION SYSTEMS

Work	Freq.	Data Rate	Range (m)	SNR (dB)	BER	Power (µW)	Energy (nJ/bit)
Ambient Backscatter [19]	539 MHz	10 kbps	0.15-1.07	X	10^{-3} to 0.7	0.79 (TX+RX)	X
BioScatter [8]	900 MHz	X	0.6-21	20-43	X	313.5	X
BLE Backscatter [9]	2.4 GHz	1 Mbps	1 to 30	X	X	1557.5	1.56
WISP [7]	915 MHz	70 kbps	4.3	X	X	1080	X
F-S Backscatter [20]	2.4 GHz	48.7 kbps	0.1 to 4.8	10 to 30	10^{-3} to 1	45	0.91
FreeRider (WiFi) [16]	2.4 GHz	20 to 60 kbps	22 to 42	X	10^{-4} to 1	30	X
WiFi Backscatter [15]	2.4 GHz	1 kbps	2.1	X	10^{-4} to 0.5	9.65	X
LoRa Backscatter [17]	868 MHz	37.5 kbps	2800	X	X	9.25	X
Underwater Backscatter [21]	20 to 40 KHz	20 kbps	62	3 to 40	10^{-4} to 0.5	120 to 500	X
Magnetic Backscatter [11]	5.95-5.96 MHz	5 kbps	0.175	X	$<10^{-3}$	730	X
Magnetoelectric Backscatter [13]	335 KHz	>1 kbps	~ 0.02	7 to 22	$<10^{-3}$	0.01	X
MIXIQ [12]	2.4 GHz	1.125 Mbps	24	X	0.1 to 0.5	300	0.31
IBID (This work)	**40 MHz**	**50 kbps**	**0.28**	**25 to 30**	10^{-3} **to** 10^{-2}	**80**	**0.28**

sensors with arbitrary placements and orientations. Achieving comparable performance layers across body locations requires careful alignment and orientation of magnetic coils and is best-suited for bracelet form factor sensors or interfacing with implanted devices directly beneath the reader's coil.

D. IBID

In contrast, IBID offers a well-balanced point in the design space, achieving a moderate data rate of 50 *kbps* and low power consumption of 80 *uW*. The receiver's signal-to-noise ratio (SNR) is comparable to existing designs, ranging between $25-30$ *dB* [8], [20], [21]. Additionally, IBID achieves a bit error rate (BER) of $\sim 10^{-3}$, which is comparable to many prior practical implementations of backscatter systems [10], [15], [16], [19], [20] while maintaining efficient energy consumption between $0.2087-0.2842 nJ/bit$ for -8 *dBm* to -11 *dBm* RF peak power. This makes IBID particularly suitable for intrabody applications where channel gain is around -30 *dB*. It outperforms existing magnetic and ultrasonic backscatter methods in terms of SNR [13], and energy efficiency [7], [8], [9], [10], [11], [12]. Finally, IBID offers potential for more robust security since the field strength highly attenuates within a few tens of centimeters from the body. These features ensure robust performance for next generation passive batteryless wearable and biomedical applications where power efficiency and communication reliability are essential.

III. IBID SYSTEM DESIGN

Figure 2(a) shows a block diagram of the IBID system which includes the IBID channel, transceiver, and the tag. Here, we model the IBID channel as a two-port network. The overall channel includes the human body, skin coupled electrodes, isolating balun, and matching network. The ports of the IBID channel are connected to the transceiver and the batteryless tag. The transceiver is connected at port 1, and the backscatter tag is connected at port 2. Here, a_1 and a_2 are the incident waves' amplitude at port 1 and port 2, respectively. b_1 and b_2 are the reflected waves' amplitude at port 1 and port 2, respectively. Both are normalized to characteristics impedance Z_0. $\Gamma_{\text{mod}}(t)$ is the modulation presented to the tag side of the channel. From standard scattering relations, $b_1(t)$ can be written as:

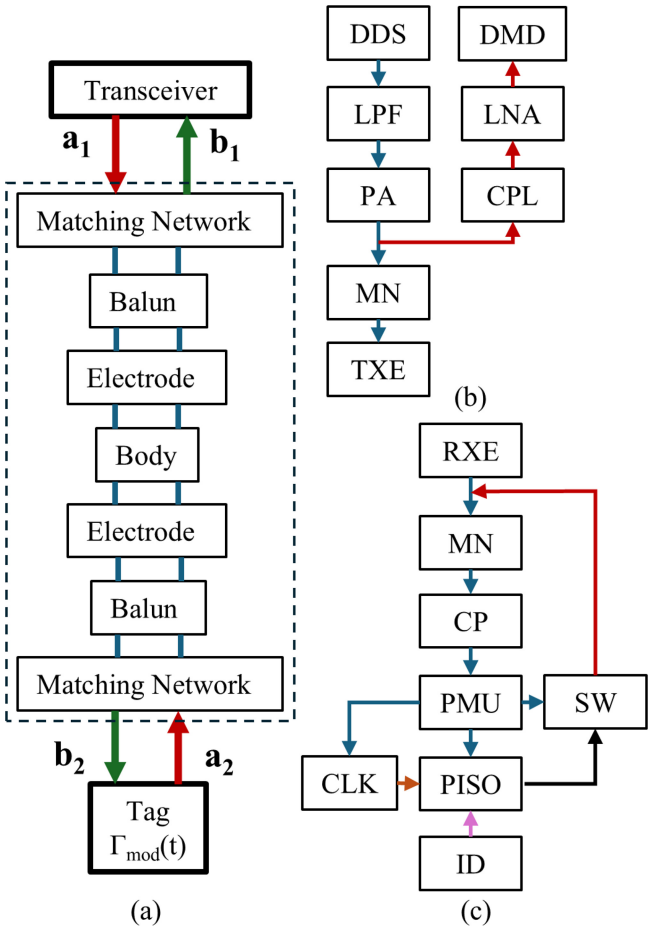

Fig. 2. Intra-body Identification System where (a) shows the two port model of the IBID channel, (b) shows the block diagram of the transceiver, and (c) shows the block diagram of the IBID tag.

$$b_1(t) = S_{11}\, a_1 \;+\; S_{12}\, \Gamma_{\text{mod}}(t)\, \frac{S_{21}\, a_1}{1 - S_{22}\, \Gamma_{\text{mod}}(t)}. \tag{1}$$

If port 1 and port 2 are well-matched, then $S_{11} \approx 0$ and $S_{22} \approx 0$, we approximate the received backscattered wave amplitude as:

$$b_1(t) \;\approx\; S_{12}\, S_{21}\, a_1\, \Gamma_{\text{mod}}(t). \tag{2}$$

Let $a_1 = A_c$ be the complex incident carrier wave from the transceiver, and $\Gamma_{\text{mod}}(t) = M(t)$ be the message signal.

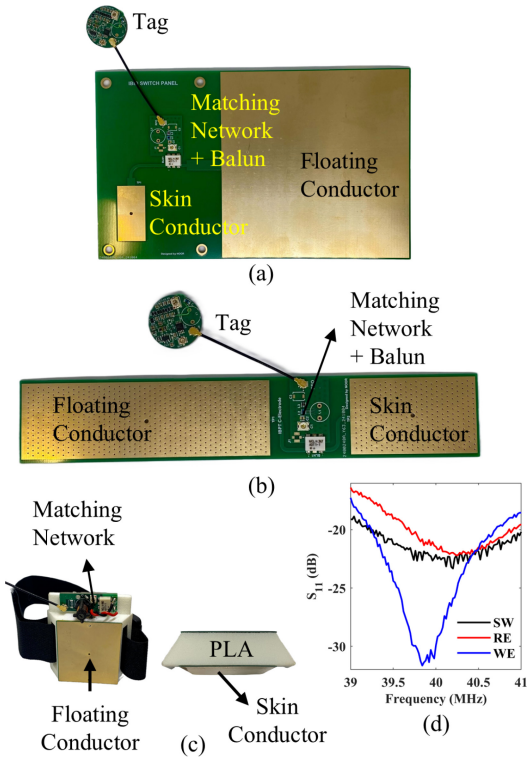

Fig. 3. (a) Instrumented switch panel (floating conductor dimension: 10×10 *cm*, skin conductor dimension:1.5×3 *cm*), (b) remote control model (floating conductor dimension:3×10 *cm*, skin conductor dimension: 3×5 *cm*), (c) interrogator electrode (30×40 *cm*), and (d) S_{11} responses of the matched skin coupled electrodes where SW denotes switch panel, RE denotes remote control, and WE denotes wrist electrode.

The received signal passes through a directional coupler characterized by the coupling factor C_{PL}:

$$b_{1,\text{coupled}}(t) = C_{PL} \cdot b_1(t) \tag{3}$$

Substituting for $b_1(t)$:

$$b_{1,\text{coupled}}(t) = C_{PL} \cdot S_{12}S_{21}A_c \cdot M(t) \tag{4}$$

which is the final backscatter expression, capturing how a time-varying load (backscatter node) at port 2 translates to a modulated reflection observed at port 1. The receiver and the demodulator processes this complex $b_{1,\text{coupled}}(t)$ signal to extract the message signal $M(t)$. The following section discusses the hardware systems of the IBID system.

A. Electrode System

There are two pairs of electrodes used in the IBID system. One electrode pair acts as the interrogator, while the other serves as the tag electrode. Figure 3(c) shows the interrogator electrode which contains a dielectric substrate (PLA plastics) of average permittivity of 3.1 and a thickness of 11 *mm*. Each electrode system comprises two conductors: a skin-coupled conductor and a floating air conductor. These conductors form a dominant loop for displacement current flow, relying on skin conductance and air capacitance over a short body channel length.

The interrogator electrode pair serves two critical functions in the IBID system: 1) powering the batteryless tag with a 40 *MHz* RF carrier injected in the intrabody capacitive loop, and 2) receives the RF energy modulated by the tag within same current loop and recovers the data transmitted by the tag. The tag electrode pair, integrated with a batteryless IBID tag, can be attached to objects of interest and does not have a fixed dielectric substrate. Here, the dielectric properties of the tag electrode will be regulated by the effective permittivity of the object composition and air. Fig. 3(d) shows the S_{11} response of the skin coupled electrodes demonstrating the impedance matching behavior with respect to 50 *ohm* for switch panel (SW), remote control model (RE), and the wrist worn interrogator electrode (WE).

B. IBID Tag

Figure 4(a) shows the printed circuit board (PCB) implementation of the IBID tag and Fig. 2(c) shows the block diagram of the tag. The tag comprises five sub-modules: the impedance matching network (MN) which matches the input of the harvester to the tag electrode pair (RXE), a 5-stage modified Dickson charge pump (CP) with a 1 *uF* storage capacitor, a power management unit (PMU), a baseband generator, and a carrier modulator using a CMOS RF switch.

An LC network is used to match the charge pump and its load to 50 *ohms* for a -10 *dBm* 40 *MHz* RF carrier. The Dickson charge pump consists of low forward drop schottky diodes (part: SMS7630). The Dickson charge pump can charge the 1 *uF* storage capacitor to approximately 2 *V* with incident power levels greater than -11 *dBm*, where the load consists of the PMU and the baseband unit.

The PMU includes a nanopower supervisor (part: TLV840NADL20DBVR) and 1.8 *V* low dropout regulator (part: TPS7A0218DBVR), providing regulated power supply to the baseband unit, oscillator (CLK) and clock divider, and the modulator. The baseband unit consists of a 100 *KHz* MEMS oscillator (part: OV-0100-C7), a low power clock divider consisting of five D-flip flops, a 16-bit parallel-in serial-out shift register (PISO), and a configurable 16-bit static ID generator using a resistive network. The output bit stream from the shift register is used as a switching signal for a high-speed MOSFET switch in the modulator. The output of the modulator is connected to the input of the impedance matching circuit to toggle between short and matched load conditions.

During operation, the tag sends a burst of IDs. Each burst consists of a stream of data packets of 16-bit length. Each bit stream is framed as a start bit, preamble bit, data bit, parity bit, and stop bit. The start bit represents the rising edge with a binary 1 level, whereas the stop bit is configured to be the falling edge with a 1-bit length. The preamble bit and the parity bit are of 3 consecutive bit lengths with high-low pattern. Apart from these fixed bits, the data bits are the variable bits with an 8-bit length.

C. IBID Transceiver

Figure 4(b) shows the transceiver hardware and Fig. 2(b) shows the block diagram of the transceiver architecture. The transceiver consists of an RF generator, microcontroller, a programmable frequency synthesizer (DDS, part: AD9851),

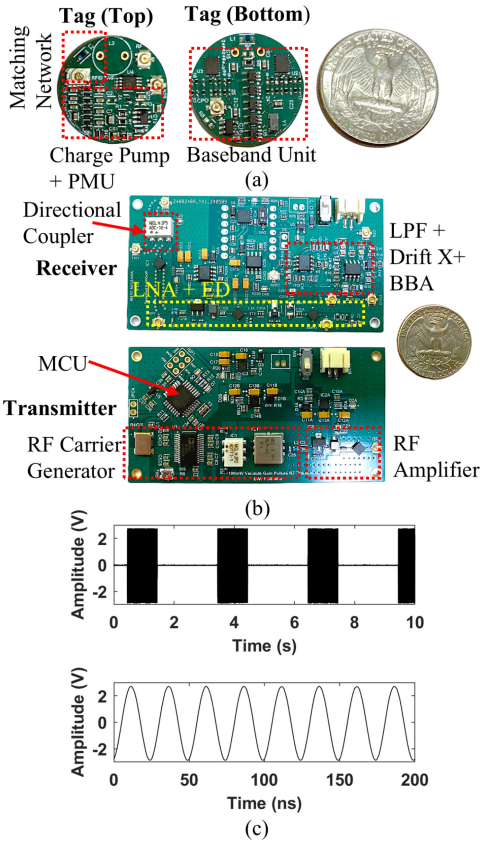

Fig. 4. PCB implementations of (a) IBID tag,(b) transceiver, and (c) transmitter output showing pulsed carrier (1 *s* ON and 2 *s* off) and waveform amplitude (+19.6 *dBm* peak power) measured with 50 *ohm* termination.

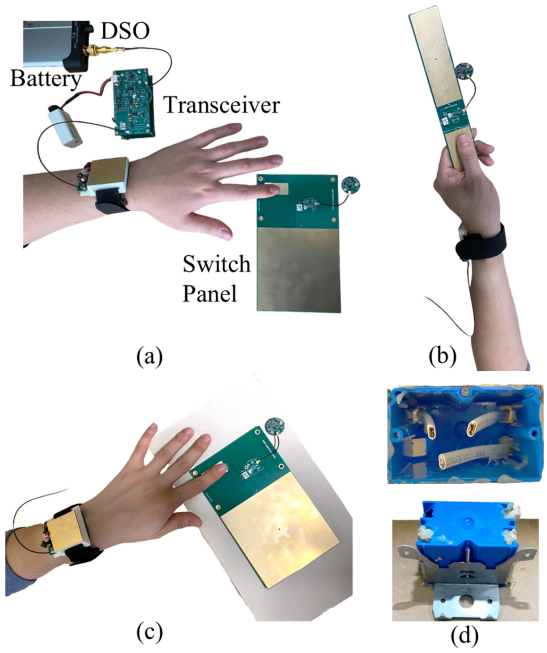

Fig. 5. (a) Experimental setup for IBID switch panel, (b) remote control, (c) switch panel over wall mount, and (d) internal view of the wall mount.

and an RF amplifier (PA, part: PHA-13LN+). The transceiver employs 33% (i.e., 1 *s* on and 2 *s* off) carrier modulation for querying the IBID tag. The receiver front-end includes a directional coupler (DC, part: ADC-10-4+), a low noise amplifier (LNA, part: PHA-13LN+), and a demodulator (DMD). The demodulator includes an envelope detector, an active second-order low-pass filter (LPF) to attenuate the carrier, a differential amplifier to cancel the DC drift (Drift X) resulting from unwanted random reflections due to movement induced impedance mismatch, and a baseband amplifier (BBA). The entire transceiver requires 5 *V* DC to operate. Figure 4(c) shows a 40 *MHz* pulsed carrier output from the transmitter with 33% duty cycle and a peak power of +19.6 *dBm*.

IV. Experimental Setup and Data Collection

This section describes the experimental setup and key signal processing steps. We provide a brief overview of the hardware configuration and environmental conditions, followed by the methods used for data post-processing and performance evaluation.

A. Experimental Setup

Figure 5(a) and Fig. 5(c) show the experimental setups for the IBID switch panel application, demonstrating both a tabletop and a wall-mounted configuration, respectively. Figure 5(b) presents the setup for the remote control and Fig. 5(d) provides a view of the internal and external construction of the wall-mount model including the wiring. We recruited ten human subjects with IRB approval, and data collection was conducted in a laboratory environment maintained at an average temperature of 20 °*C* and 24% relative humidity.

B. Data Collection and Signal Processing

To evaluate the performance of IBID, a tag backscatters a burst of ID packets instead of a single packet thus enabling performance studies over short time intervals while achieving statistically significant channel measurements. Additionally, since our currently system offers a uni-directional communication channel (Tag to Transceiver), burst transmissions create multiple opportunities for successful packet reception, greatly increasing the probability that one ID is successfully decoded. This repetition allows us to employ a simplified digital infinite impulse response (IIR) filter with fewer coefficients. This results in an improved signal-to-noise ratio (SNR) and more robust bit-stream reconstruction. Furthermore, a burst results in multiple received ID packets which allows for a reliable statistical characterization of channel bit error rate (BER) and energy consumption, which is essential for optimizing future iterations of our IBID system beyond simple ID transmission. During data collection, the output from the baseband amplifier in the demodulator unit of the transceiver is recorded using a battery-operated digital storage oscilloscope (part: OWON VDS6102) with a bandwidth of 100 *MHz*, a sampling rate of 1 gigasamples per second, and 8-bit analog-to-digital converter resolution. The data from the oscilloscope is saved on a battery-operated laptop (part: Lenovo Chrome Book 11.6 inch) using a USB cable. A MATLAB script was written to perform offline digital signal processing on the stored data.

We process raw data obtained from the oscilloscope by correcting DC offset and convert to the frequency domain using a fast Fourier transform. Since our baseband frequency is a fixed 50 *KHz*, we use a second-order Butterworth bandpass filter to isolate the desired frequency band (i.e., 40–150 *kHz*). After filtering, the discrete Fourier transform is recomputed using a fast Fourier transform to analyze the refined spectrum and determine whether filter parameters need adjustment. Figure 6(a) and Fig. 6(b) illustrate an example of the ac coupled raw baseband signal in the time domain and frequency domain, respectively which were obtained from a subject using switch panel model on a table. The spectrum response of the raw signal reveals low frequency noises lower than 30 *KHz*. Figure 6(c) and Fig. 6 (d) show the time domain and frequency spectrum of the filtered demodulated baseband signal. The filtered spectrum show the fundamental frequency of 50 *KHz* with lower and upper sidebands of 46.9 *KHz* and 53.1 *KHz*.

We found that the second order butterworth filter works well for all of our collected dataset since we are processing a burst of ID instead of a single packet. Previous work such as ambient backscatter has used a moving average filter for processing baseband signal [19]. However, the butterworth filter is more frequency selective and provides stronger noise attenuation than a moving average filter. For both raw signal and the filtered signal, the signal-to-noise ratio (SNR) is calculated by evaluating the fundamental frequency and its first sidebands (lower and upper) as a signal – this metric enables an understanding of the effectiveness of the filter in attenuating noise. However, to characterize the receiver, we report the SNR values obtained from raw demodulated signals.

Finally, a time segment containing the filtered baseband signal is compared to a threshold value (e.g., the midpoint of the positive envelope of the filtered AC coupled signal) to extract binary bit stream. Later, we computed bit error rate by counting the binary bit stream data with respect to the total transmitted bits within a finite burst length. Figure 6(e) and Fig. 6(f) show the time domain and frequency spectrum of the 16-bit binary bitstream within a packet. The frequency spectrum shows progressive harmonics of square pulses. Figure 7(a) shows a burst of raw data packets during one charge cycle of the 1 *uF* storage capacitor obtained from a test subject interacting with the remote control model. Figure 7(b) and Fig. 7(c) are the filtered and digitized consecutive packet streams observed in a single burst.

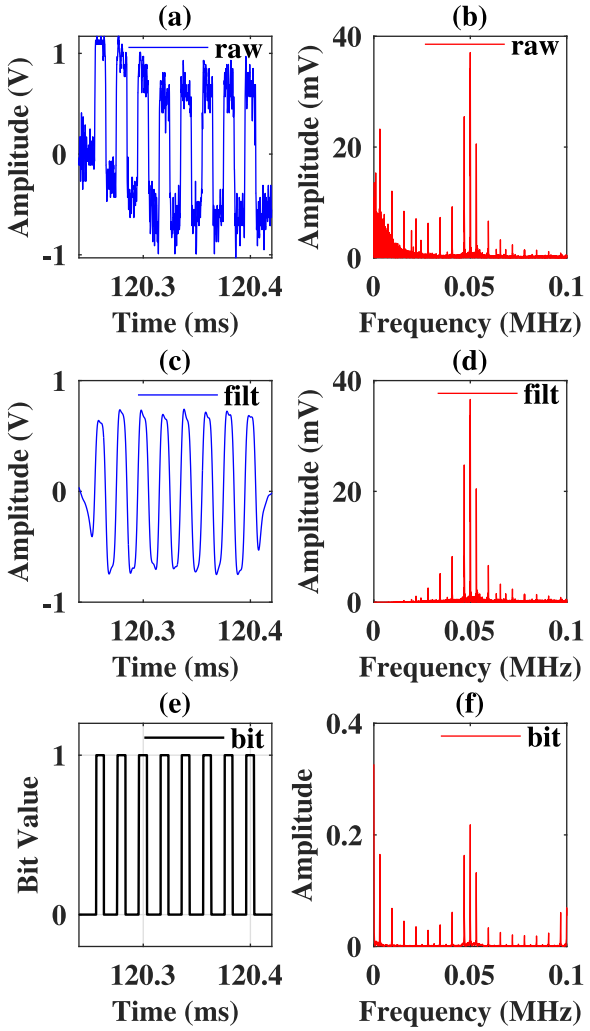

Fig. 6. (a),(b) time domain signal and frequency spectrum of raw data packet (AC coupled), (c),(d) time domain signal and frequency spectrum of filtered signal, and (e),(f) time domain signal and frequency spectrum of recovered bit stream within a burst obtained from a switch panel model.

V. Results

In this section, we evaluate the performance of the proposed IBID system through several analyses. First, we examine the relationship between the signal-to-noise ratio (SNR) and communication range to determine its effective operating distance. We then assess SNR variations among human subjects, showcasing the system's robustness against intra-body and inter-body variations. Bit-level statistics are provided to demonstrate data transmission reliability. Finally, we analyze the Bit Error Rate (BER) relative to SNR to illustrate communication accuracy and BER as a function of confidence intervals for statistical reliability. We also quantify latency against received RF power at the tag, highlighting system responsiveness under energy constraints. Finally, we measure the tag's power consumption, affirming IBID's suitability for ultra-low-power wearable and implantable applications. These metrics collectively characterize IBID's performance and effectiveness for reliable intra-body communication.

A. SNR vs Range Analysis

Figure 8 displays SNR measurements (in dB) as a function of distance (in cm) across 10 human subjects (S1 through S10) using three experimental setups. Subjects provided data across different channel lengths ranging from 8 *cm* to 28 *cm* driven by individual anatomical constraints such as length of the forearm and palm. Across individual subjects, SNR readings generally range from 20 *dB* to 30 *dB*. However, two measurements in Fig. 8(a), such as S1 at 23 *cm* and S10 at 27 *cm*, fall below 20 *dB*, indicating significant variations. We assume these outliers are due to differences in body orientation, distance, or environmental factors.

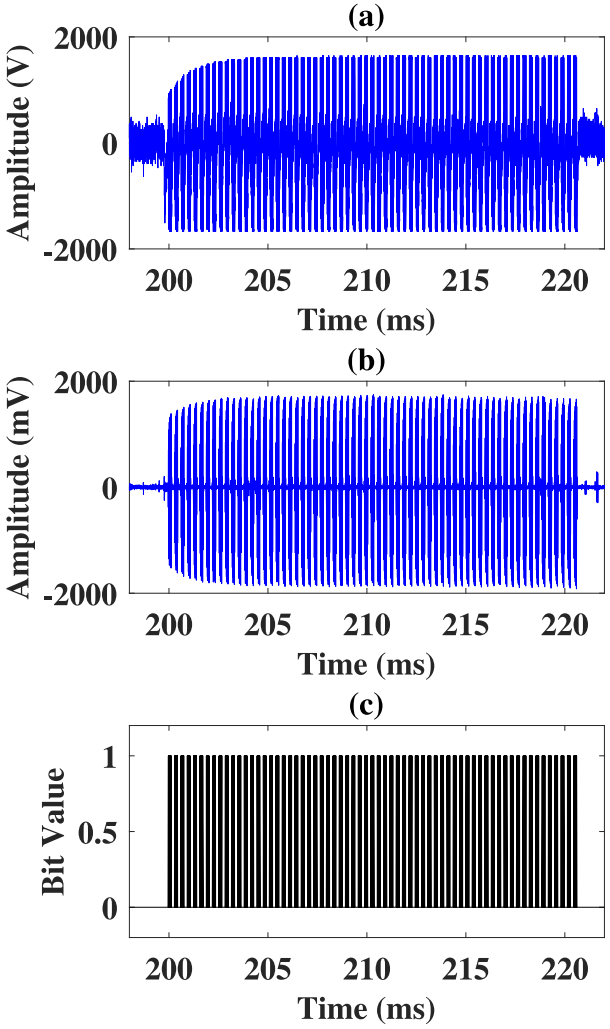

Fig. 7. (a) Received burst of data packets during one charge-discharge cycle of 1 *uF* storage capacitor (AC coupled), (b) filtered signal, and (c) recovered bit stream within a burst obtained from the remote control model.

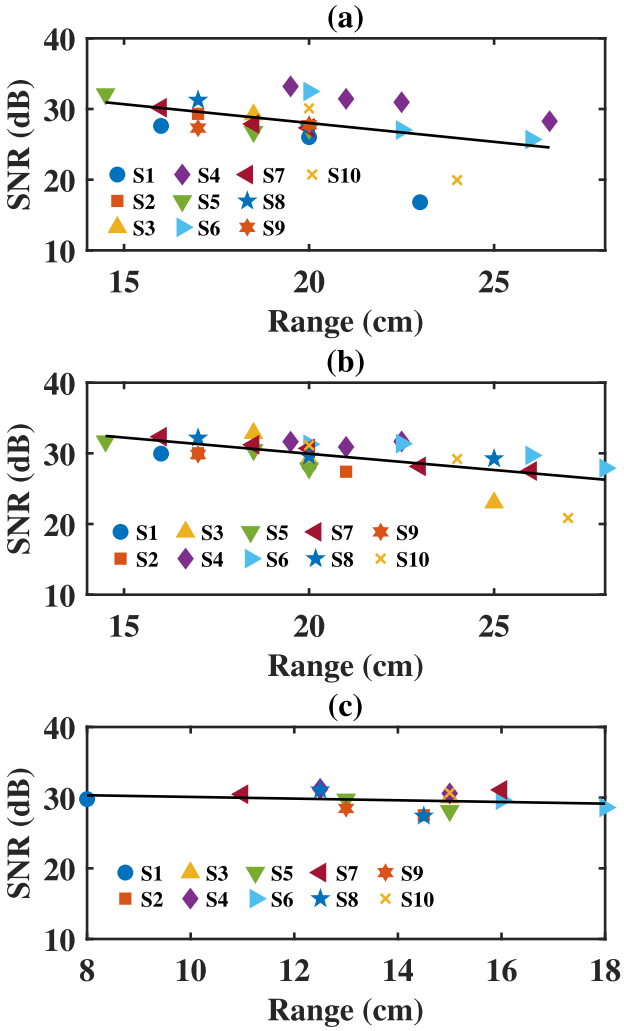

Fig. 8. (a) Signal to noise ratio (SNR) vs range data obtained from ten human subjects using the (a) switch panel model over table, (b) switch panel model over wall mount, and (c) remote control model.

In Figure 8(a) (model: switch panel over table), the slope is $-0.53\ dB/cm$ with an R^2 value of 0.19. For Fig. 8(b) (model: switch panel over wall mount), the slope is $-0.46\ dB/cm$ and R^2 is 0.39, while in Fig. 8(c) (model: remote control), the slope is $-0.12\ dB/cm$ and R^2 is 0.05.

The linear regression in Fig. 8 indicate a nonlinear relationship between the SNR and the range, as evidenced by the low R^2 values observed in all experiments. While increased distance typically leads to decreased SNR, other factors such as body positioning and environmental conditions significantly influence the results. For instance, a subject's hands rested on the table in the switch panel model, but were elevated in the wall-mounted and remote control models.

B. SNR vs Subject Analysis

Figure 9 shows the average signal-to-noise ratio (SNR) for each subject across the three hardware configurations (i.e., switch panel over table (E1), switch panel over wall mount (E2), and remote control (E3)). We observe inter-subject and intra-subject variability, quantified by the mean and standard deviation of SNR. For instance, Subject S1 has a relatively low mean SNR of 23.48 *dB* in the E1 experiment with a high standard deviation of approximately 5.83 *dB*. However, in the E2 and E3 experiments, the mean SNR increases to around 29 *dB*, accompanied by much smaller standard deviation. Similarly, Subject S10 displays a broad standard deviation of 7.18 *dB* in the E2 experiment, indicating a wide range of readings.

It is also important to note that certain cases show a standard deviation of zero. This occurs when there is only one measurement for a specific subject-experiment pairing (e.g., S2 in E1, S3 in E1, and S9 in E2), resulting in no variability.

From this experiment, we observe some subjects, such as S4, consistently achieved higher signal-to-noise ratios (SNRs). In contrast, subjects like S1 and S10 experienced significant reductions in SNR under certain conditions or at greater distances. These differences represent the complexity of real-world scenarios due to inter-body variations. Nonetheless, the system consistently maintained adequate SNR levels for reliable communication.

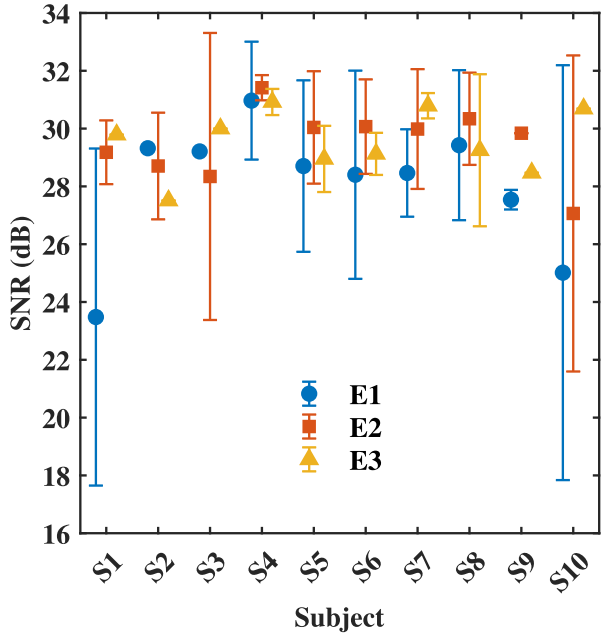

Fig. 9. Signal to noise ratio (SNR) statistics obtained from ten subjects using the switch panel model over a table (E1), switch panel model over the wall mount (E2), and remote control model (E3).

C. Bit Statistics

In Fig. 10, we show the number of transmitted bits and error bits across three experiments (E1, E2, and E3) involving subjects S1 to S10 at various distances ranging from approximately 8 *cm* to 28 *cm*.

In general, the E2 (switch panel over wall mount) experiment tends to produce fewer or no errors for many subjects. In contrast, the E1 (switch panel over table) experiment occasionally exhibits larger error counts at distances of 20 *cm* to 24 *cm*. The results from the E3 (remote control model) experiment are also varied.

It is evident that Subject S7 transmits the most data overall (9,504 bits) with 20 errors, while Subject S9 transmits the fewest (3,648 bits) with 6 errors. In total, the dataset includes 66,352 transmitted bits and 200 errors across all subjects and experiments, reflecting an overall bit error rate of 0.30%.

D. BER vs SNR

Figure 11 presents the measurements of Signal-to-Noise Ratio (SNR) and Bit Error Rate (BER) as a percentage (%) across ten subjects and three experiments: E1 (Fig. 11(a)), E2 (Fig. 11(b)), and E3 (Fig. 11(c)). Most SNR values fall within the 25 *dB* to 34 *dB* range; however, there are exceptions, S10 in SW-table reaches a BER of 3.02% at 19.94 *dB* (not shown in Fig. 11(a) due to y-axis scaling), while subject S4 exhibits a 1.18% error rate at 28.27 *dB*. Apart from that, most BER entries record values under 1%.

Several subjects show zero BER in specific setups, with subjects S3, S4, S5, and S9 all having multiple instances with 0% error. This suggests that they might have operated under short distances, stable orientations, or otherwise favorable conditions. On the other hand, moderate error rates, typically

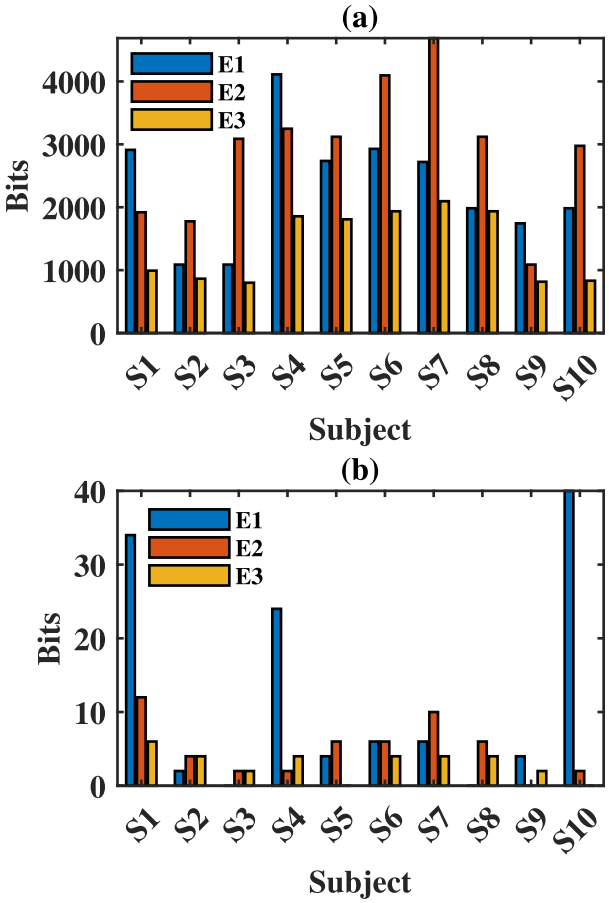

Fig. 10. (a) Received bit counts, and (b) error bit counts obtained from ten subjects using the switch panel model over a table (E1), switch panel model over the wall mount (E2), and remote control model (E3).

ranging from 0.2% to 0.7%, are common for SNR values in between 25 *dB* to 34 *dB* (e.g., S1, S2, S7). This pattern indicates a moderate level of link reliability.

E. BER and Confidence Interval Analysis

The Wilson Score Interval was used to calculate the confidence interval for the bit error rate (BER) because it provides accurate estimates, especially with low observed probabilities or small sample sizes. Unlike normal approximation, it avoids overly narrow or negative intervals at extreme values, making it more reliable for assessing BER by considering the error proportion and sample size.

The Wilson Score confidence interval is calculated using:

$$\text{CI} = \frac{p + \frac{z^2}{2n} \pm z\sqrt{\frac{p(1-p)}{n} + \frac{z^2}{4n^2}}}{1 + \frac{z^2}{n}} \tag{5}$$

Here, p is the BER (probability of error), n is the number of transmitted bits, and z is the z-score for the desired confidence level, with $z = 1.96$ for a 95% confidence interval.

Figure 12 shows channel bit error rates (BER) with Wilson confidence intervals at a 95% confidence level across all 10 subjects. Confidence interval (CI) values are obtained for each subject and experiment (E1, E2, E3) and averaging multiple CI entries using the mean function. Most entries

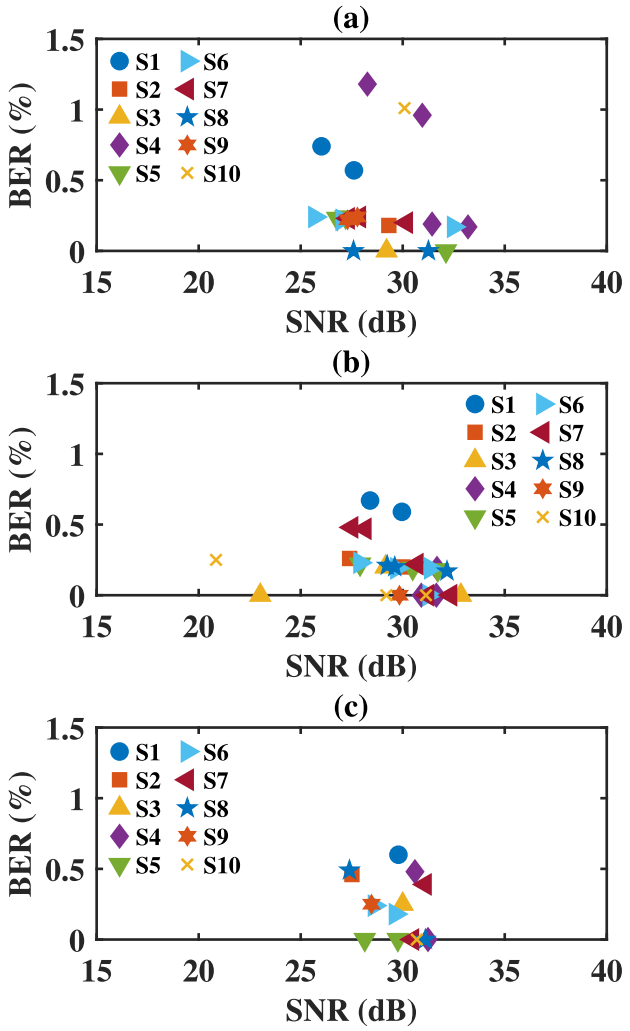

Fig. 11. Comparison of bit error rate to signal-to-noise ratio across ten human subjects from the (a) switch panel model over a table, (b) switch panel model over the wall mount, and (c) remote control model.

report BER values below 1%, with lower bounds often near zero, especially for those showing no observed errors. The upper bounds can range from approximately 0.30% to 0.90%. However, there are several measurements that stand out due to higher observed BER, such as S1 at 2.6% with a confidence interval up to approximately 3.99%.

Moderate BER values, ranging from 0.2% to 0.5%, typically have upper confidence bounds of around 0.7% to 1.2%. This suggests that although observed errors are relatively low, the true BER could be slightly higher based on statistical variability.

F. Latency vs. Tag's Received RF Power

Figure 13 shows the outputs of the charge pump and the baseband generator at peak RF input power levels of -10 *dBm*. Here, the input RF power is generated from a 50 *ohm* RF signal generator and injected at the RF input port of the designed IBID tag. The charge pump output demonstrates a peak before stabilizing, while the baseband output shows periodic ID bursts. We have observed similar output responses

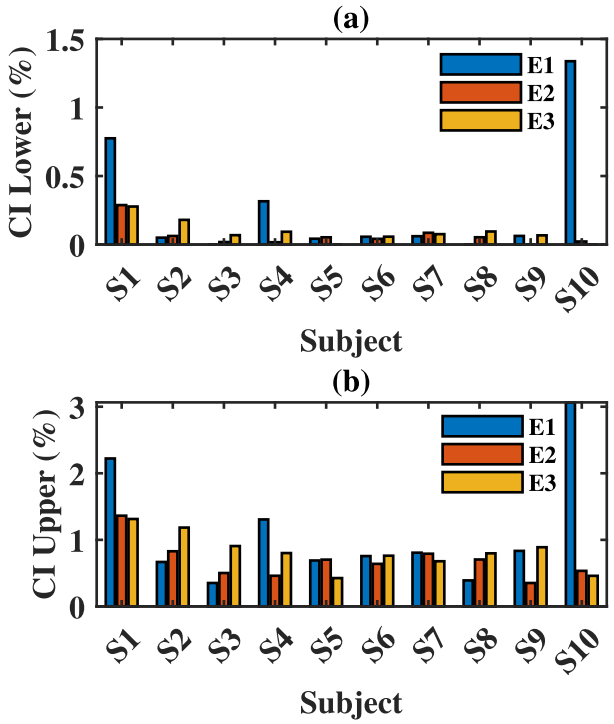

Fig. 12. Confidence interval analysis of the bit error rate (BER) using the Wilson score interval across ten human subjects for three experimental setups: the switch panel model on a table (E1), the switch panel model mounted on a wall (E2), and the remote control model (E3). (a) Represents the lower confidence interval, while (b) depicts the upper confidence interval results across all subjects.

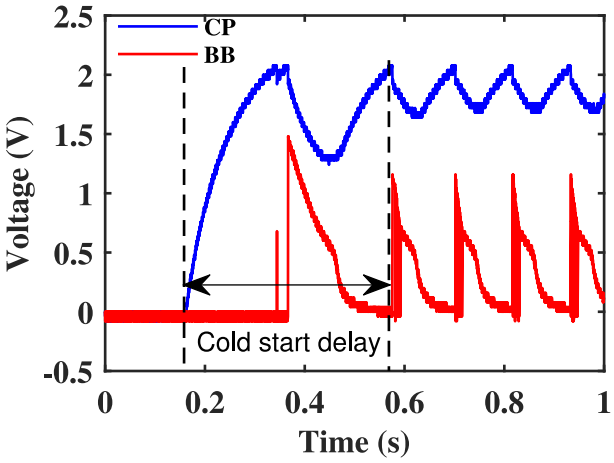

Fig. 13. Charge pump (CP) output and baseband (BB) output at a peak RF power input of -10 *dBm* to the IBID tag.

for -8 *dBm*, -9 *dBm*, and -11 *dBm*. Below -11 *dBm*, the charge pump output becomes less than 2 *V*, and the PMU unit does not activate the baseband generator.

Figure 14 shows the cold start delay of 0.4190*s* for -10*dBm*, and 1.4609*s* for -11*dBm*. This trend indicates that lower received RF power results in a longer delay before the baseband output is activated, as the charge pump requires more time to accumulate sufficient energy.

Since backscattering relies on modulating an incident signal, any delay in the charge pump reaching its operational threshold

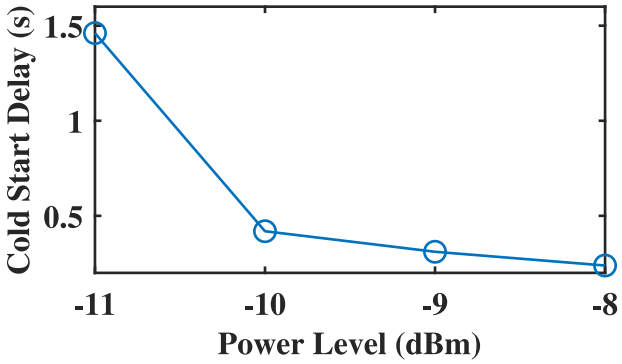

Fig. 14. Cold start delay observed at different RF peak power levels.

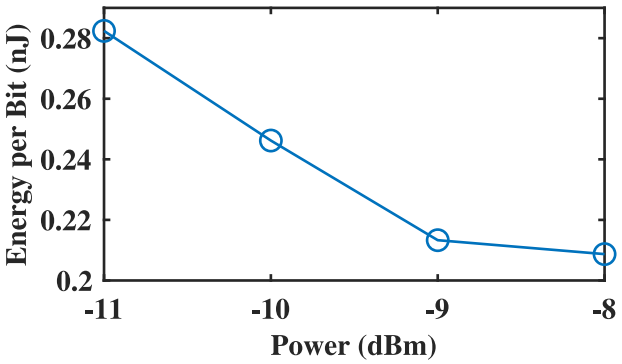

Fig. 15. IBID tag's energy consumption per bit observed at different RF peak power levels.

results in a delayed system response and roundtrip latency. This delay would also be large for a brief duty cycle of the carrier compared to a continuous wave transmission.

G. Tag's Power Consumption

Our final result quantifies an IBID tag's energy consumption per bit is determined by measuring the energy stored in a capacitor during a burst transmission. First, the total number of bits transmitted is calculated based on the burst duration for each power level. Then, the energy per bit (E_{bit}) can be expressed as:

$$E_{\text{bit}} = \frac{E_{\text{cap}}}{N_{\text{bits}}} \tag{6}$$

where,

$$E_{\text{cap}} = \frac{1}{2}C\left(V_H^2 - V_L^2\right) \tag{7}$$

$$N_{\text{bits}} = N_{\text{packets}} \times N_{\text{bits per packet}} \tag{8}$$

Here, C is the capacitance value, V_H and V_L are the high and low capacitor window voltages, N_{packets} is the number of packets in the measurement interval, and $N_{\text{bits per packet}}$ is the number of relevant data bits per packet.

Figure 15 shows the calculated energy consumption per bit for passive IBID tags at various input peak RF power levels. At -11 *dBm*, the energy per bit was highest at 0.2824 nJ/bit. This value gradually decreased to 0.2462 nJ at -10 *dBm*, 0.2133 nJ/bit at -9 *dBm*, and reached the lowest 0.2087 nJ/bit at -8 *dBm*.

VI. Discussion

In this section we discuss ongoing challenges and future work planned for IBID. First, we discuss the ability of IBID cope with external electromagnetic interference, then discuss our plans for implementing a complete IBID communication stack that builds on the physical layer foundation presented in this manuscript.

A. Coping With Body-Coupled Electromagnetic Interference

We conducted a brief study of the impact of electromagnetic interference (EMI) on the receiver. Figure 16 shows the receiver output with DC offset corrected under various environmental conditions, excluding backscatter effects. Figure 16(a) and Fig. 16(b) display the time-domain and frequency-domain responses for a 50 *ohm* resistive load connected directly to the transceiver output, recorded under ambient lighting. In Fig. 16(c) and Fig. 16(d), the transceiver output was connected to a skin-coupled, impedance-matched electrode in a room with reduced natural ambient light. In this scenario, considerable noise concentrated in the $0 - 30$ *kHz* frequency range. However, when two proximate light sources were activated (overhead LED desk lighting), the receiver output exhibited pronounced periodic modulation with a peak amplitude of about 1.5 *V* (as shown in Fig. 16(e)). The frequency spectrum (Fig. 16(f)) reveals a strong fundamental frequency component around 48 *kHz* and multiple harmonic components. Since minimal noise was detected when attached to a 50 *ohm* load, this indicates the receiver itself does not generate considerable interference. However substantial noise is detected when attached to a skin-coupled impedance-matched IBID electrode, and in the bright illumination case, interferes with the 50 *KHz* baseband frequency. This suggests that external electromagnetic interference is coupled through the electrode interface since our electrode system acts as a high quality tuned LC circuit. More distant room scale lighting also significantly contributes to the overall noise floor, implying the presence of indirect coupling mechanisms.

Prior work has demonstrated that visible light from artificial sources can leak RF signals [22] that originate from the upper harmonics of high frequency switching regulators. These RF signals can be easily coupled into our electrode system and create undesirable carrier modulation. It is likely that any external interferer which has a frequency spectrum of tens of MHz will also interfere with the tuned IBID electrode through fundamentals or strong harmonics. These findings highlight the receiver's vulnerability to environmental interference when paired with wearable electrodes, emphasizing a need for improved shielding, selective noise filtering, channel selection, or mixing additional baseband subcarriers that result in offset frequencies offset from the noise source(s).

B. IBID Protocol Design

This work characterizes the physical layer performance of a first-of-its-kind intra-body backscatter identification (IBID) system. However, a comprehensive intra-body backscatter communication solution requires further development of

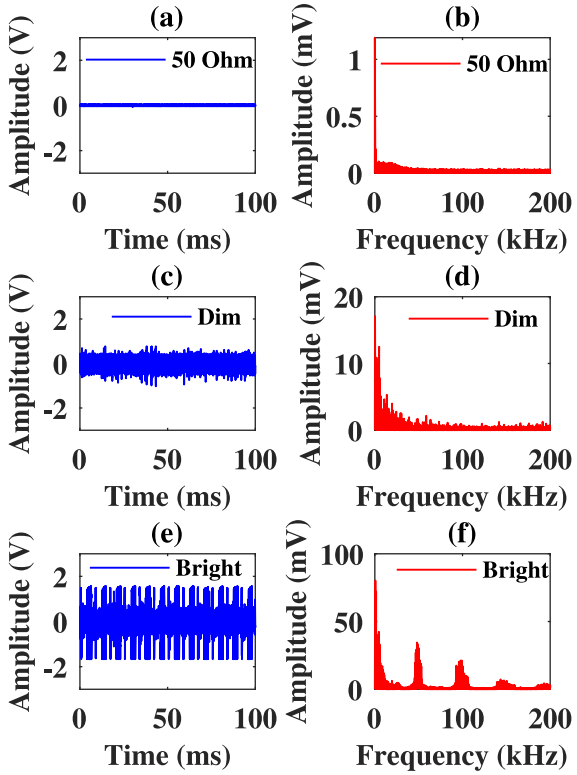

Fig. 16. Receiver output observed for (a,b) 50 *ohm* transceiver load under no artificial light, (c,d) skin-coupled electrode under dim artificial light, and (e,f) skin-coupled wrist electrode with two nearby bright artificial light sources.

higher protocol layers. Our next steps are to design and implement custom Medium Access Control (MAC) and application layers inspired by RFID standards (i.e., EPC Gen2 [23]), but adapted to intra-body communication constraints and guided by the results obtained in this manuscript. The revised protocol will maintain a reader-driven, query-based architecture optimized for capacitively coupled body channel communication. It will implement dynamic power management for batteryless operation and self-clocked encoding such as FM0. Anti-collision, adaptive scheduling, and session management will support reliable multi-tag identification and network management. Furthermore, lightweight data encoding and error correction will ensure efficient, secure communication within intrabody devices under strict energy and latency constraints which can minimize packet retransmissions while ensuring a reliable communications channel.

C. Ongoing Challenges

Despite the advancements presented in this work, RFID backscatter technology on the human body still faces several significant challenges [24]. Path attenuation and the intra-body effect [1], [2] can reduce received power by detuning tag antennas. This would be a significant problem for a narrow-band antenna system which demands specialized designs for improved performance. Additionally, environmental interference and multipath effects can compromise signal reliability due to reflections and competing wireless signals. While intrabody power, security and privacy concerns [25], [26] persist due to the minimalist hardware design of these systems, making encryption difficult and leaving them vulnerable to attacks. To tackle these challenges, our ongoing research concentrates on developing better antenna designs, receiver and tag design, advanced signal processing methods, and improved protocols to make body-worn RFID systems more practical and scalable for human body applications.

VII. Conclusion

Our comprehensive analysis across ten subjects shows that intra-body backscatter identification (IBID) communication provides reliable and energy-efficient performance. It allows a maximum transmission range of 28 *cm* and consumes 0.28 nJ/bit at -11 *dBm* peak RF power. Measurements showed consistently high SNR averaging between 25 to 30 *dB*, translating to low overall bit error rates (BER) of approximately 0.3%. Despite moderate variability due to subject positioning and environmental influences, shorter distances yielded significantly improved reliability. These quantitative metrics indicate IBID's efficiency and practical viability for battery-free identification tasks. Future work will involve adapting a modified EPC Gen2-inspired communication protocol optimized for intra-body applications to further enhance system functionality and reliability.

References

[1] N. Mohammed, R. W. Jackson, J. Gummeson, and S. I. Lee, "Wireless intra-body power transfer via capacitively coupled link," in *Proc. IEEE-EMBS Int. Conf. Wearable Implant. Body Sensor Netw. (BSN)*, 2022, pp. 1–4.

[2] N. Mohammed, R. Wang, R. W. Jackson, Y. Noh, J. Gummeson, and S. I. Lee, "ShaZam: Charge-free wearable devices via intra-body power transfer from everyday objects," *Proc. ACM Interact., Mobile, Wearable Ubiquitous Technol.*, vol. 5, no. 2, pp. 1–25, 2021.

[3] R. Shukla, N. Kiran, R. Wang, J. Gummeson, and S. I. Lee, "SkinnyPower: Enabling batteryless wearable sensors via intra-body power transfer," in *Proc. 17th Conf. Embed. Netw. Sensor Syst.*, 2019, pp. 68–82.

[4] J. Park, H. Garudadri, and P. P. Mercier, "Channel modeling of miniaturized battery-powered capacitive human body communication systems," *IEEE Trans. Biomed. Eng.*, vol. 64, no. 2, pp. 452–462, Feb. 2017.

[5] A. Datta, M. Nath, D. Yang, and S. Sen, "Advanced biophysical model to capture channel variability for EQS capacitive HBC," *IEEE Trans. Biomed. Eng.*, vol. 68, no. 11, pp. 3435–3446, Nov. 2021.

[6] N. Mohammed, R. W. Jackson, S. I. Lee, and J. Gummeson, "IBID: Intra-body identification using capacitive backscatter," in *Proc. IEEE Int. Conf. RFID Technol. Appl. (RFID-TA)*, 2024, pp. 54–57.

[7] A. P. Sample, D. J. Yeager, P. S. Powledge, A. V. Mamishev, and J. R. Smith, "Design of an RFID-based battery-free programmable sensing platform," *IEEE Trans. Instrum. Meas.*, vol. 57, no. 11, pp. 2608–2615, Nov. 2008.

[8] W. Jiao, Y. Li, X. Xi, J. Wang, D. Fang, and X. Chen, "BioScatter: Low-power sweat sensing with backscatter," in *Proc. 21st Annu. Int. Conf. Mobile Syst., Appl. Services*, 2023, pp. 191–204.

[9] J. F. Ensworth and M. S. Reynolds, "BLE-backscatter: Ultralow-power IoT nodes compatible with Bluetooth 4.0 low energy (BLE) smartphones and tablets," *IEEE Trans. Microw. Theory Tech.*, vol. 65, no. 9, pp. 3360–3368, Sep. 2017.

[10] J. Jang and F. Adib, "Underwater backscatter networking," in *Proc. ACM Special Interest Group Data Commun.*, 2019, pp. 187–199.

[11] B. Tao, E. Sie, J. Shenoy, and D. Vasisht, "Magnetic backscatter for in-body communication and localization," in *Proc. 29th Annu. Int. Conf. Mobile Comput. Netw.*, 2023, pp. 1–15.

[12] M. Rostami, X. Chen, Y. Feng, K. Sundaresan, and D. Ganesan, "MIXIQ: Re-thinking ultra-low power receiver design for next-generation on-body applications," in *Proc. 27th Annu. Int. Conf. Mobile Comput. Netw.*, 2021, pp. 364–377.
[13] Z. Yu et al., "Magnetoelectric backscatter communication for millimeter-sized wireless biomedical implants," in *Proc. 28th Annu. Int. Conf. Mobile Comput. And Netw.*, 2022, pp. 432–445.
[14] D. Vasisht, G. Zhang, O. Abari, H.-M. Lu, J. Flanz, and D. Katabi, "In-body backscatter communication and localization," in *Proc. Conf. ACM Special Interest Group Data Commun.*, 2018, pp. 132–146.
[15] B. Kellogg, A. Parks, S. Gollakota, J. R. Smith, and D. Wetherall, "Wi-Fi backscatter: Internet connectivity for RF-powered devices," in *Proc. ACM Conf. SIGCOMM*, 2014, pp. 607–618.
[16] P. Zhang, C. Josephson, D. Bharadia, and S. Katti, "Freerider: Backscatter communication using commodity radios," in *Proc. 13th Int. Conf. Emerg. Netw. Exp. Technol.*, 2017, pp. 389–401.
[17] V. Talla, M. Hessar, B. Kellogg, A. Najafi, J. R. Smith, and S. Gollakota, "LoRa backscatter: Enabling the vision of ubiquitous connectivity," *Proc. ACM Interact., Mobile, Wearable Ubiquitous Technol.*, vol. 1, no. 3, pp. 1–24, 2017.
[18] Q. Wang, Q. Guan, J. Cheng, and Y. Tang, "Ultrasonic backscatter communication for implantable medical devices," *IEEE Trans. Mol., Biol. Multi-Scale Commun.*, vol. 8, no. 4, pp. 292–296, Dec. 2022.
[19] V. Liu, A. Parks, V. Talla, S. Gollakota, D. Wetherall, and J. R. Smith, "Ambient backscatter: Wireless communication out of thin air," *ACM SIGCOMM Comput. Commun. Rev.*, vol. 43, no. 4, pp. 39–50, 2013.
[20] P. Zhang, M. Rostami, P. Hu, and D. Ganesan, "Enabling practical backscatter communication for on-body sensors," in *Proc. ACM SIGCOMM Conf.*, 2016, pp. 370–383.
[21] R. Ghaffarivardavagh, S. S. Afzal, O. Rodriguez, and F. Adib, "Ultra-wideband underwater backscatter via piezoelectric metamaterials," in *Proc. Annu. Conf. ACM Special Interest Group Data Commun. Appl., Technol., Archit., Protocols Comput. Commun.*, 2020, pp. 722–734.
[22] M. Cui, Q. Wang, and J. Xiong, "Bracelet+: Harvesting the leaked RF energy in VLC with wearable bracelet antenna," in *Proc. 20th ACM Conf. Embed. Netw. Sensor Syst.*, 2022, pp. 250–262.
[23] M. Burmester and B. De Medeiros, "The security of EPC Gen2 compliant RFID protocols," in *Proc. 6th Int. Conf. Appl. Cryptogr. Netw. Secur. (ACNS)*, New York, NY, USA, 2008, pp. 490–506.
[24] J. Wang, L. Chang, O. Abari, and S. Keshav, "Are RFID sensing systems ready for the real world?" in *Proc. 17th Annu. Int. Conf. Mobile Syst., Appl., Services*, 2019, pp. 366–377.
[25] Z. Luo, W. Wang, J. Xiao, Q. Huang, T. Jiang, and Q. Zhang, "Authenticating on-body backscatter by exploiting propagation signatures," *Proc. ACM Interact., Mobile, Wearable Ubiquitous Technol.*, vol. 2, no. 3, pp. 1–22, 2018.
[26] P. J. Hawrylak and J. Hale, "Data privacy issues with RFID in healthcare," in *Medical Data Privacy Handbook*. Cham, Switzerland: Springer, 2015, pp. 549–567.

Noor Mohammed is currently pursuing the Ph.D. degree with the Department of Electrical and Computer Engineering, University of Massachusetts Amherst. His research focuses on intra-body wireless power transfer, backscatter communication through human body, wearable sensors, and RFID technologies, with an emphasis on batteryless systems for health monitoring and human-computer interaction.

Robert W. Jackson (Life Fellow, IEEE) received the Ph.D. degree from Northeastern University in 1981. He joined the faculty of the University of Massachusetts in 1982, where he is currently a Professor of Electrical and Computer Engineering. His primary research and teaching interests center on microwave and millimeterwave electronics, especially integrated circuits. In particular, he has contributed in the areas of electromagnetic modeling of high frequency integrated circuits, novel circuit structures, and packages for microwave and millimeterwave integrated circuits. His current interests include miniature, low cost devices for sensing applications, active antennas, and high frequency CMOS. He is a member of the packaging technical committee for the Microwave Theory and Techniques Society. He has served on technical program committees for the International Microwave Symposium and the conference on Electrical Performance of Electronic Packaging, and was the co-general chair of the latter for 2004 and 2005. He was an Associate Editor of the IEEE TRANSACTIONS ON MICROWAVE THEORY AND TECHNIQUES 2008 to 2010.

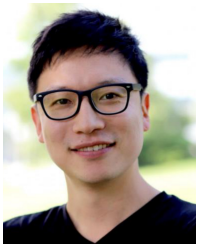

Sunghoon Ivan Lee (Senior Member, IEEE) is an Associate Professor with the College of Information and Computer Sciences, University of Massachusetts Amherst. He directs the Advanced Human and Health Analytics Lab. His research focuses on mobile and personalized health technologies, including wearable sensing, embedded systems, and data analytics for individuals with neurological and movement disorders. He is a recipient of the NSF CRII and NIH Trailblazer Awards.

Jeremy Gummeson received the Ph.D. degree in computer systems engineering from the University of Massachusetts Amherst (UMass Amherst) in 2013. He is an Assistant Professor with the Department of Electrical and Computer Engineering, UMass Amherst, with an adjunct appointment with the Manning College of Information and Computer Sciences. Before joining UMass, he held research positions with Hewlett Packard Labs and Disney Research. His research focuses on energy-efficient and battery-free sensing systems, including energy harvesting, backscatter communication, and human-centric wireless sensing. He has served as a reviewer for top-tier conferences and journals in mobile computing and RFID systems.